UCLA
UCLA Previously Published Works

Title
Integrative genomic analysis of mouse and human hepatocellular carcinoma

Permalink
https://escholarship.org/uc/item/6rj4k1k9

Journal
Proceedings of the National Academy of Sciences of the United States of America, 115(42)

ISSN
0027-8424

Authors
Dow, Michelle
Pyke, Rachel M
Tsui, Brian Y
et al.

Publication Date
2018-10-16

DOI
10.1073/pnas.1811029115

Peer reviewed

eScholarship.org Powered by the California Digital Library
University of California

Integrative genomic analysis of mouse and human hepatocellular carcinoma

Michelle Dow[a,b,c], Rachel M. Pyke[a,b], Brian Y. Tsui[a,b], Ludmil B. Alexandrov[d,e,f], Hayato Nakagawa[g], Koji Taniguchi[h,i,j,k], Ekihiro Seki[l,m], Olivier Harismendy[c,f,m], Shabnam Shalapour[h,i,j], Michael Karin[h,i,j,1], Hannah Carter[a,f,n,1], and Joan Font-Burgada[o,1]

[a]Division of Medical Genetics, Department of Medicine, University of California, San Diego, La Jolla, CA 92093; [b]Bioinformatics and Systems Biology Graduate Program, University of California, San Diego, La Jolla, CA 92093; [c]Health Science, Department of Biomedical Informatics, School of Medicine, University of California, San Diego, La Jolla, CA 92093; [d]Department of Cellular and Molecular Medicine, University of California, San Diego, La Jolla, CA 92093; [e]Department of Bioengineering, University of California, San Diego, La Jolla, CA 92093; [f]Moores Cancer Center, University of California, San Diego, La Jolla, CA 92093; [g]Department of Gastroenterology, Graduate School of Medicine, The University of Tokyo, 113-8655 Tokyo, Japan; [h]Laboratory of Gene Regulation and Signal Transduction, School of Medicine, University of California, San Diego, La Jolla, CA 92093; [i]Department of Pharmacology, School of Medicine, University of California, San Diego, La Jolla, CA 92093; [j]Department of Pathology, School of Medicine, University of California, San Diego, La Jolla, CA 92093; [k]Department of Microbiology and Immunology, Keio University School of Medicine, Tokyo 160-8582, Japan; [l]Department of Medicine, Cedars-Sinai Medical Center, Los Angeles, CA 90048; [m]Department of Medicine, School of Medicine, University of California, San Diego, La Jolla, CA 92093; [n]Cancer Cell Map Initiative, University of California, San Diego, La Jolla, CA 92093; and [o]Cancer Biology Program, Fox Chase Cancer Center, Philadelphia, PA 19111

Contributed by Michael Karin, August 30, 2018 (sent for review June 28, 2018; reviewed by Kenneth W. Kinzler and Michael Lawrence)

Cancer genomics has enabled the exhaustive molecular characterization of tumors and exposed hepatocellular carcinoma (HCC) as among the most complex cancers. This complexity is paralleled by dozens of mouse models that generate histologically similar tumors but have not been systematically validated at the molecular level. Accurate models of the molecular pathogenesis of HCC are essential for biomedical progress; therefore we compared genomic and transcriptomic profiles of four separate mouse models [MUP transgenic, TAK1-knockout, carcinogen-driven diethylnitrosamine (DEN), and Stelic Animal Model (STAM)] with those of 987 HCC patients with distinct etiologies. These four models differed substantially in their mutational load, mutational signatures, affected genes and pathways, and transcriptomes. STAM tumors were most molecularly similar to human HCC, with frequent mutations in *Ctnnb1*, similar pathway alterations, and high transcriptomic similarity to high-grade, proliferative human tumors with poor prognosis. In contrast, TAK1 tumors better reflected the mutational signature of human HCC and were transcriptionally similar to low-grade human tumors. DEN tumors were least similar to human disease and almost universally carried the *Braf* V637E mutation, which is rarely found in human HCC. Immune analysis revealed that strain-specific MHC-I genotype can influence the molecular makeup of murine tumors. Thus, different mouse models of HCC recapitulate distinct aspects of HCC biology, and their use should be adapted to specific questions based on the molecular features provided here.

hepatocellular carcinoma | mouse models | cancer mutational landscapes | comparative genomics | immune analysis

Primary liver cancer is the fifth most common cancer worldwide but is the second leading cause of cancer deaths, being associated with very poor prognosis (1). Hepatocellular carcinoma (HCC) accounts for 85–90% of all primary liver cancers (1, 2). In most cases, HCC presents as a double disease since it is usually accompanied by cirrhosis caused by a variety of risk factors. Globally, HCC epidemiology is driven by chronic hepatitis B virus (HBV) and hepatitis C virus (HCV) infections, which account for 80% of cases (3, 4). Other major risk factors include alcohol, aflatoxin, parasites, obesity, and genetic disorders. Incidence trends have been changing across the globe depending on regional variations in the prevalence of underlying etiologies. For instance, incidence rates in the United States have tripled from 1977–1979 to 2005–2007 (5). Furthermore, 30–35% of HCC patients in the United States do not have viral infection. Nonalcoholic fatty liver disease and its advanced presentation, nonalcoholic steatohepatitis (NASH), are emerging as the driving force behind this growth. Current estimates project that 1.5–2% of the United States population has cirrhosis due to NASH, and this is expected to become the leading indication for liver transplantation in the not-so-distant future (6). Considering the annual cumulative incidence of HCC in NASH cirrhosis (6), an upsurge of new HCC cases is expected in the United States in the coming decades. Analogous trends are expected in regions that have similar socioeconomic characteristics with coinciding increases in obesity rates.

Potential curative treatment (surgical resection and transplantation) is indicated for 30–40% of HCC patients, while the remaining 60–70% of patients are eligible only for palliative and symptomatic treatment (7). The sole targeted therapy for HCC is the pan-kinase inhibitor sorafenib, affecting Raf kinases and VEGF and PDGF receptors, indicated for patients with advanced diseases (8). However, the response to sorafenib is dismal, and the median overall survival is extended by only 2.8 mo (9). A similar small increase in overall survival has been observed with another Food and Drug Administration-approved pan-kinase inhibitor, regorafenib (10). However, nivolumab, a programmed cell death protein-1 (PD-1) immune checkpoint inhibitor, has shown promising effects for patients who failed to respond to sorafenib (11).

Significance

Hepatocellular carcinoma (HCC) research has been hampered by the absence of consensus mouse models with clearly defined molecular features faithfully recapitulating human HCC. Here we tackle this gap by implementing a cross-species comparative analysis between a large cohort of patients and four diverse mouse models focused on clinically and therapeutically relevant aspects of genomic and transcriptomic profiles and propose two of these models as valid for the study of different stages of human HCC.

Author contributions: M.D., M.K., H.C., and J.F.-B. designed research; M.D., H.C., and J.F.-B. performed research; M.D., R.M.P., B.Y.T., L.B.A., H.N., K.T., E.S., O.H., and S.S. contributed new reagents/analytic tools; M.D., R.M.P., B.Y.T., L.B.A., H.C., and J.F.-B. analyzed data; and M.D., L.B.A., M.K., H.C., and J.F.-B. wrote the paper.

Reviewers: K.W.K., The Sidney Kimmel Comprehensive Cancer Center; and M.L., The Broad Institute of MIT and Harvard.

The authors declare no conflict of interest.

Published under the PNAS license.

Data deposition: The data have been deposited in the Sequence Read Archive (SRA), NCBI (https://www.ncbi.nlm.nih.gov/Traces/study/?acc=SRP159121; accession no. PRJNA488497, study no. SRP159121).

[1]To whom correspondence may be addressed. Email: karinoffice@ucsd.edu, hkcarter@ucsd.edu, or joan.font-burgada@fccc.edu.

This article contains supporting information online at www.pnas.org/lookup/suppl/doi:10.1073/pnas.1811029115/-/DCSupplemental.

Due to the complex links between different risk factors and HCC development, the molecular drivers and combinations thereof involved in hepatocarcinogenesis are still poorly understood. Previous studies have characterized the transcriptomic landscape of HCC tumors, identifying expression signatures associated with HBV, TP53 signaling, and WNT or AKT pathway activation (12). Genomic analyses have identified major pathways altered in HCC, such as the WNT, PIK3/Ras, and cell-cycle pathways (13, 14), and more recent studies have characterized mutational signatures associated with diverse risk factors such as alcohol consumption, smoking, and exposure to aflatoxin B1, as well as putative driver genes including telomerase reverse transcriptase (TERT) promoter mutations, TP53, CTNNB1, and AXIN1 (15–18). Among the largest HCC cohort studies are The Cancer Genome Atlas (TCGA) and the International Cancer Genome Consortium (ICGC), which together have undertaken four independent projects to help catalog the molecular alterations found in HCC patients (19, 20). HCC genetic aberrations show substantial heterogeneity, likely reflecting effects of etiology, ethnicity, and environmental exposures. Remarkably, the genetics of NASH-induced HCC remains poorly characterized.

The development of well-defined mouse models of HCC that accurately reproduce human disease has been a priority and is essential for studying basic tumor biology and therapeutic response. However, dozens of HCC mouse models have been developed by different interventions. Several carcinogens have historically been used, such as diethylnitrosamine (DEN), carbon tetrachloride (CCl4), 2-acetylaminofluorene (2-AAF), thioacetamide (TAA), and aflatoxins, among others, with large variations in protocols for dosage and dosage schedule, use of tumor promoters, and different genetic backgrounds all producing phenotypic variations. The alternative, genetically modified mice, encompasses two main categories, one in which a genetic alteration produces chronic tissue damage that spontaneously generates HCC and a second group in which different oncogenic variants or tumor suppressors are introduced specifically into all or a subset of hepatocytes. Other models include tumor cell implantation or complex systems to recapitulate chronic infections by HBV and HCV (21). An early attempt to characterize the similarity of 68 tumors from seven HCC mouse models and 91 human HCC samples based on gene-expression microarrays found that some mouse models shared gene-expression patterns similar to those of HCC patients with good prognosis and others had gene-expression patterns similar to those of HCC patients poor prognosis (22), but the analysis was limited to expression data and evaluated mouse models rarely used in HCC studies. Unfortunately, the genetic makeup of full-blown HCC in mouse models is generally unknown, and therefore it is unclear which animal models are molecularly more similar to human disease. Thus, the large multiplicity of models and the inconsistency in experimental parameters along with their unknown genetic component have obscured a better understanding of HCC biology. In addition, our current knowledge of human NASH-induced HCC is limited, and although some mouse models have been proposed, most do not replicate the complete spectrum of clinical features and have been poorly characterized molecularly (23).

Here, we provide a comprehensive comparative genomics characterization of mouse HCC in four independent mouse models and four human HCC cohorts. We catalog mutational signatures, mutated genes, and pathways together with the associated transcriptional perturbations to determine mouse–human similarities. This work uncovers the benefits and limitations of the use of mouse models of HCC and provides a reference to better tailor future mouse research on HCC and preclinical studies to reflect the molecular characteristics of the human disease.

Results

Somatic Mutational Signatures. Genomic and transcriptomic profiles were obtained for tumors from four different mouse models of HCC: DEN (24, 25), TAK1Δ^{HEP} (TAK1) (25, 26), MUP-uPA + high-fat diet (MUP) (27), and STAM (28), which rely on different approaches to induce liver tumors within 9 mo (except for the STAM model, in which tumors develop within 5 mo) (Table 1). The DEN model has been widely used for its ease and consistency in generating tumors. However, this model does not present with common risk factors for human HCC, such as chronic liver injury or fibrosis. Conversely, the TAK1 model induces HCC in the context of a microenvironment highly similar to that in HCC patients with chronic liver disease. The MUP and STAM models are designed to mimic NASH-induced HCC. The MUP model reproduces all the clinical features of human NASH, but most of the tumors appear "adenoma-like," while the STAM model rapidly develops NASH-like cirrhosis in the absence of obesity with rapid development of HCCs histologically similar to human disease.

We performed whole-exome sequencing (WES) on a total of 56 mouse tumors and six normal spleens reaching an average coverage depth of 100× (minimum 70×) (*SI Appendix*, Table S1*A*). Initially, we sequenced nine samples from each model with 10 additional samples sequenced at a later date for the STAM and DEN models, based on these models' greater potential for generating insights into HCC mutagenesis. To systematically compare the properties of somatic alterations observed in mouse models with those found in human patients, human HCC exome-based (total n = 987; from LICA-CN, LICA-FR, LIHC-US, and LINC-JP; n = 163, 234, 377, and 213, respectively) and genome-based (total n = 314; from LICA-FR, LIHC-US, LINC-JP, and LIRI-JP, n = 5, 53, 28, and 228, respectively) somatic mutation data were retrieved from the ICGC data portal (19) and TCGA (20).

We identified somatic mutations in the four mouse models by comparing tumor DNA with splenic DNA for each model. Median somatic mutation rates in MUP and TAK1 mice were similar to those observed in human HCCs (two or three mutations per megabase) while the DEN mice had a much higher median burden of somatic mutations (~27 mutations per megabase), as expected of a well-characterized carcinogen (Fig. 1*A*, *Left*). Strikingly, the STAM model had on average a fivefold higher mutation rate than that observed in the DEN model (~122.56 mutations per megabase). We also observed large differences in the somatic mutation profiles in the different mouse models (Fig. 1*B*, *Left*). The DEN model had a very low rate of C→G transversions (mutations are referred to by the pyrimidine nucleotide of the Watson–Crick base pair), and fewer C→T transitions but an excess of T→A transversions. The TAK1 model had a notable excess of T→G transversions, and the STAM model mutational profile was dominated by C→T transitions relative to all other categories. The differences are likely due to the diverse mechanisms by which HCCs are induced in these models. For example, mice in the DEN model are treated with diethylnitrosamine, a carcinogen found in tobacco smoke, and mice in the STAM model are treated with streptozotocin to impair pancreatic B cell function (28) and are fed a high-fat diet (HFD) to recapitulate NASH-associated cirrhosis. In contrast, the TAK1Δ^{HEP} and MUP-uPA models are transgenic mouse models relying on the induction of chronic hepatocyte injury with spontaneous hepatocarcinogenesis. Thus, mutations in these models are expected to accumulate more slowly, through chronic injury and inflammatory processes, than in models with acute exposure to DNA-damaging agents.

Among human cohorts, we observed a fairly consistent median somatic mutation rate in the range of two to three mutations per megabase except for the LINC-JP cohort, which had a higher median rate of 6.26 mutations per megabase (Fig. 1*A*, *Right*). This cohort includes samples from HCC patients treated with cisplatin, a chemotherapy drug that cross-links DNA to inhibit replication and cause apoptosis and that is associated with a higher burden of mutations (19, 29). Further, signature 12 was highly elevated in LINC-JP compared with other cohorts (threefold elevation; Wilcoxon signed-rank test; P value 1.65e-14). The etiology of signature 12 remains unknown, and this elevation might reflect an environmental mutagen that is more prevalent in Japan. The mutation profiles of the four human exome-sequencing cohorts were also similar; however, we observed an excess of T→A transversions

Table 1. Description of mouse models

Mouse model	Treatments/traits	HFD	Chronic damage	Cirrhosis	Time to cancer, mo	Histology	No. samples
DEN	Carcinogen; diethylnitrosamine	No	No	No	9	Histologically hard to classify	9 + 10
MUP	MUP-driven expression of uPA only in hepatocytes	Yes	Yes	Yes (mild)	9	Adenoma-like, low malignancy	9
STAM	Streptozocin in WT mice; insulin deficiency	Yes	Yes	Yes (severe)	5	Malignant phenotype, human-like features	9 + 10
TAK1	Genetic deletion of *TAK1* gene in liver	No	Yes	Yes	9	Adenoma-like, low malignancy	9

in the LICA-CN cohort which was less prevalent in the LIHC-US cohort. Furthermore, a higher rate of C→T transitions was observed in the LIHC-FR cohort, and a slightly elevated rate of T→G transversions was found in the LIHC-JP and LIHC-US cohorts (Fig. 1*B*, *Right*). Overall, the observed variation in mutation rates and spectra suggest that different factors drive mutagenesis in the various mouse models. While human tumors look less heterogeneous, there were still differences in the abundance of certain base substitutions.

The somatic mutations in a cancer genome are the results of the activity of multiple mutational processes. Previously, more than 30 characteristic patterns, termed "mutational signatures," of single-nucleotide substitutions have been found across human cancer, and many of them have been attributed to the activity of endogenous and/or exogenous carcinogens. To determine the signatures of the mutational processes operative in the cancer genomes of the four mouse models, we decomposed the single-nucleotide substitutions in their immediate context (i.e., 96 possible classes of mutations) into mutational signatures. We applied the method described by Alexandrov et al. (30) across all 56 mouse samples and identified five distinct signatures (A, B, C, D, and E) (*SI Appendix*, Fig. S1*A* and Table S1*B*), four of which corresponded (cosine similarity greater than 0.92) to signatures previously reported in humans (31). Signature A was different from any previously observed mutational signatures in human cancer (maximum cosine similarity of 0.76) and was specific to the DEN samples; thus, this signature is likely associated with exposure to diethylnitrosamine. Signature B corresponded to human signature 44 (cosine similarity = 1.0), which is attributable to a known sequencing artifact. Two signatures, C and D, were dominated by an alkylating agent-specific signal; signature C was most similar to human signature 11 (cosine similarity = 1.0) and was found predominantly in STAM mice but also in a few other samples. The remarkably high mutation rate of STAM tumors and the strong signature of an alkylating agent suggest that streptozotocin is a potent carcinogen of the liver. Signature D was observed mostly in MUP and in some TAK1 samples and shared similarity with human signature 12, previously associated with HCC (cosine similarity = 0.93). Signature E, present in the four mouse models, was similar to two as yet unexplained human signatures (signatures 19 and 32). Given that the mutation profiles of the DEN and STAM models are dominated by mutations attributable to mutagens, the more subtle contributions of other mutagenic processes may be masked in these samples (*SI Appendix*, Fig. S1*B*).

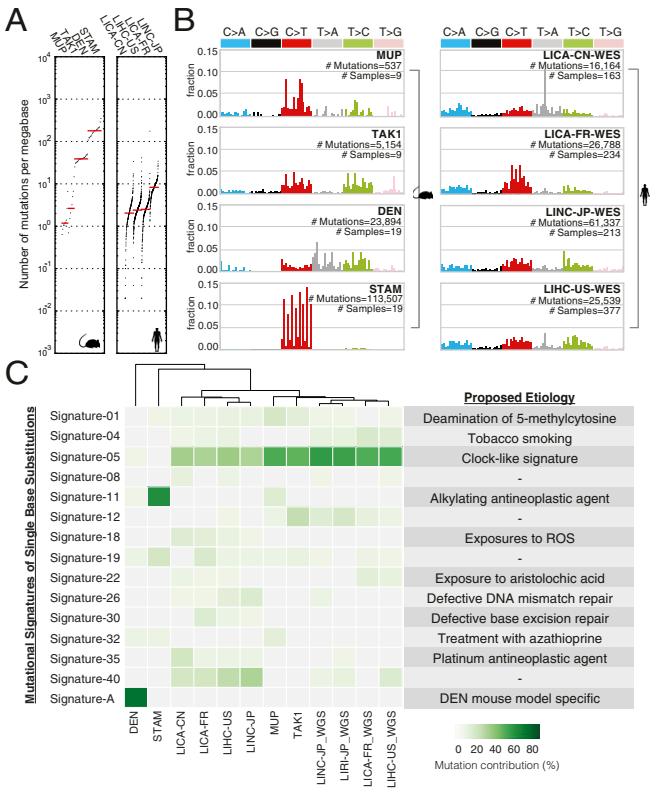

Fig. 1. Mutational profiles for the human and mouse cohorts and corresponding mutagenic signatures. (*A*) Mutational burden of mouse models and human HCC patient cohorts (WES). Design inspired by Lawrence et al. (37). (*B*) Nucleotide substitutions for each cohort were binned into 96 categories by combining the six possible base substitutions (C→A, C→G, C→T, T→A, T→C, and T→G) with 5′ and 3′ flanking bases, following the standard/alphabetic order of trinucleotides. Human cohorts are separated by geographical origins of the ICGC data. (*C*) Mutation contributions (%) for the identified signatures are shown for each human and mouse cohort. Signatures are shown if they account for >5% of mutations in one or more of the 12 cohorts.

We next sought to determine how similar the mutation profiles observed in mouse models are to known mutational signatures previously reported in human HCC. We used a supervised approach that attempts to find the weighted combination of existing signatures that best explains a mutation profile (*Methods*). After mapping mutational profiles for mouse models and human cohorts to known human mutational signatures (32), we clustered the groups based on overall similarity of the signature weights (Fig. 1*C* and *SI Appendix*, Fig. S1*C*). Mutational signatures have previously been analyzed in several human HCC cohorts (15, 17, 33), implicating several signatures in human HCC, including 4, 6, 16, 22, 23, and 24. Our analysis revealed similar patterns of mutation signature across human cohorts with clear cohort-specific risk factors (Fig. 1*C*). While all human cohorts were dominated by signature 5, known to correlate with age in liver (32, 34), the LICA-FR whole-genome sequencing (WGS) cohort was most strongly associated with a smoking signature, with the LIHC-US WGS showing weaker evidence of similar exposures. In contrast, the LICA-CN cohort showed stronger influence of a signature attributed to reactive oxygen species compared with other human cohorts.

Interestingly, signatures 1, 5, and 19 were seen almost universally across both human and mouse models. While signature 5 accounted for a high proportion of mutations in most samples, only small proportion of mutations was attributed to signatures 1 and 19. Nevertheless, all three signatures were found in most human HCC WES, WGS, MUP, and TAK1 samples. Signatures 1 and 5 are associated with clock-like mutational processes

accumulating with age, while the etiology of signature 19 remains unknown. Most signatures were observed only in human HCCs (signatures 4, 8, 18, 22, 26, 30, 35, and 40) or only in mouse HCCs (signatures 11, 32, and mouse signature A). As expected, the STAM model was dominated by signature 11, which is associated with exposure to alkylating agents, and mutations in the DEN model were predominantly attributable to the DEN-specific mutagenic signature. Although DEN is a carcinogenic compound found in tobacco smoke, its mutational signature has not been observed in human cancers associated with tobacco smoking. Rather, the predominate pattern of somatic mutations in cancers associated directly with tobacco exposure is signature 4, which has been experimentally matched with exposure to benzo(*a*)pyrene (35). Interestingly, the MUP and TAK1 models were associated with signature 12, which was also observed in all the human WGS cohorts.

Mutations in mouse models thus strongly reflect the etiology of HCC in the model, with some etiologies creating mutation profiles that differ widely from those in human disease. Human HCCs have the most diversity in mutational signatures among human cancers (17), potentially reflecting the liver's central role in metabolism and detoxification and its unique physiology, being the first organ to receive blood influx from the intestinal tract. Thus, the liver is potentially the target of a wide variety of tissue-damaging agents as well as mutagens, which may account for the molecular heterogeneity of human HCC.

Somatically Altered Genes. Despite considerable differences in mutation signatures between human HCC and mouse models, the resulting mutations could nonetheless impact common genes in both species, causing disease through similar mechanisms. To evaluate this hypothesis, we analyzed the occurrence of mutations in 17,046 genes that are 1:1 orthologs in human and mouse, which included 92% of solid-tumor–relevant genes (*Methods*) from the cancer gene census (CGC) (31). Consistent with previous reports (20, 36), we observed considerable heterogeneity in somatic alterations across human HCC tumors. *TP53* and *CTNNB1*, the most frequently mutated genes, were mutated in only ∼20–25% of tumors, without significant co-occurrence (*SI Appendix*, Fig. S2*A*), while other known cancer genes were mutated in fewer than 10% of tumors. Among the top 10 significantly mutated genes (MutSigCV, $q < 0.1$), only *CTNNB1* showed significantly different patterns of mutation between human HCC cohorts (*SI Appendix*, Fig. S2*B*), with >20% of tumors in three of four cohorts harboring *CTNNB1* mutations but only 2% of LICA-CN tumors having *CTNNB1* mutations. Across human cohorts, MutSigCV (37) identified 13 genes with higher-than-expected mutation rates: *TP53*, *CTNNB1*, *AXIN1*, *ALB*, *BAP1*, *EEF1A1*, *NFE2L2*, *RPS6KA3*, *CDKN2A*, *RB1*, *ACVR2A*, *KEAP1*, and *ARID1A*.

We next mapped all somatic single nucleotide variants (SNVs) and indels obtained for mouse models to annotated genes. Overall, the MUP and TAK1 mouse models had very few nonsynonymous mutations (n = 306 and 876, respectively), whereas the STAM and DEN models showed much higher numbers (n = 83,910 and 17,859, respectively), consistent with the observed somatic mutation rates in these models. We therefore sought to identify genes enriched for positive signatures of selection for each mouse model. Since MutSigCV requires large sample sizes (37), we used an alternative method to identify significantly mutated genes (SMGs) (*Methods*) that seeks to detect a bias toward mutations expected to perturb protein activity by using the ratio of nonsynonymous to synonymous mutations (38). In total, we evaluated 12,995 genes and identified 377 SMGs across mouse models; of these SMGs, one was found in the MUP model (*Hist1h4j*, ortholog of human *HIST1H4K*), 25 were found in the DEN model, and 351 were found in the STAM model (Dataset S1). In total, 11 of the 377 SMGs were previously implicated cancer genes in the CGC: *Abl1*, *Bcl9l*, *Cbl*, *Foxa1*, *Mycn*, *Nutm1*, *Olig2*, *Tert*, *Tshr*, *Braf*, and *Sh2b3*.

Since the mutated genes in the STAM and DEN models far exceeded the average number of mutated genes in human HCC, we concluded that most detected SMGs could be the result of the high mutation rate caused by the mutagenic agents used in these models. As a first step to simplify the analysis, we focused the mouse–human comparison on the subset of tier 1 and 2 cancer-driving genes in the CGC. *SI Appendix*, Fig. S3 summarizes the total alterations observed in each mouse model, contrasting mutation frequencies across mouse and human HCC tumors. Again, the majority of mutations in CGC genes were contributed by the DEN and STAM models that have extremely high mutation rates. Importantly, although only CGC genes were considered, a large proportion of mutations had very low CHASM (Cancer-specific High-throughput Annotation of Somatic Mutations) scores (39), indicating that many of their mutations are likely to be passenger mutations. We therefore sought to eliminate likely passenger mutations in CGC genes using a liver cancer-specific CHASM classifier. Mutations were ranked according to CHASM score, and a cutoff was selected that retained only highly probable driver mutations [false-discovery rate (FDR) ≤0.1] unless previously documented in human tumors in the COSMIC (Catalog of Somatic Mutations in Cancer) database. This was repeated for human cohorts, with the additional condition that samples from the four studies were removed from COSMIC. After this procedure, we compared mutation frequencies of human–mouse CGC orthologs to evaluate potential similarities. In general, most of the top 31 most frequently mutated genes in human tumors were also found to be frequently mutated across mouse models (Fig. 2*A*). However, although *TP53* was the most frequently mutated gene across human HCCs, it was mutated in only 2 of the 56 mouse tumors. *CTNNB1*, the second most commonly mutated gene in human HCC, was mutated at a comparable frequency in the STAM model (26%), but no mutations were observed in the other

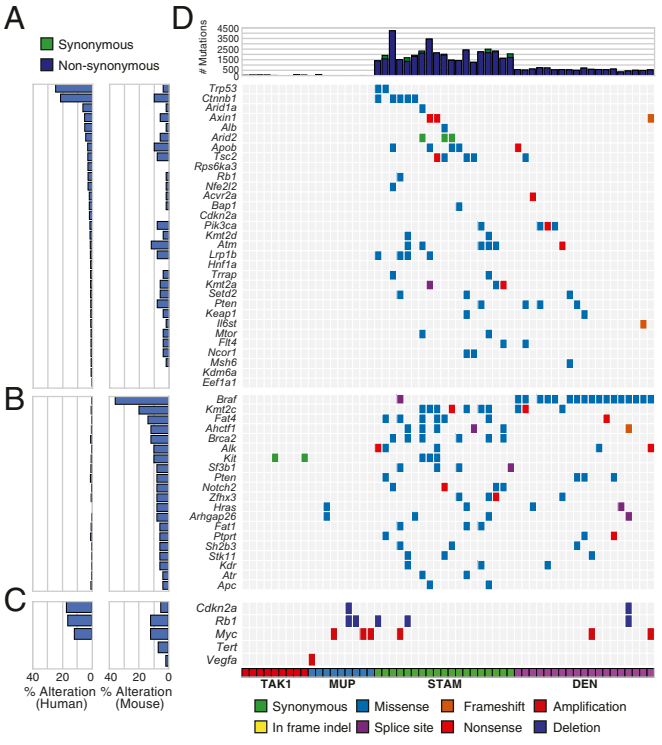

Fig. 2. The driver landscape of four HCC mouse models. (*D*, *Upper*). The bar plot shows unfiltered individual tumor mutation rates across tumors. (*Lower*) Mutational effects (synonymous, missense, and others) are indicated for each gene and sample. Silent mutations were excluded unless the identical mutation was observed in multiple independent mouse tumors. The mouse models are identified by a color bar at the bottom of the figure. (*Left*) Bar plots show human and mouse alteration frequencies across frequently mutated genes from human HCC cohorts (*A*), frequently mutated cancer genes in the four mouse models (*B*), and SCNAs of genes in mouse which overlapped with recurrent SCNAs previously reported in human HCC (*C*).

three models. *Ctnnb1* mutations mostly corresponded to recognized driver mutations in human *CTNNB1*, including S33F, G34E, T41I, and D32N (Dataset S1*B*). Interestingly, we also observed a higher overall mutation rate in mouse tumors of several known cancer genes (31) that were rarely mutated in human HCC (Fig. 2*B* and *SI Appendix*, Fig. S3*B*). Most notable among these was *BRAF*, which was mutated in 17 of 19 DEN tumors, all carrying the V637E substitution that is equivalent to the human V600E mutation.

Somatic DNA copy-number alterations (SCNAs) have also been implicated in human HCC pathogenesis. Previous HCC studies have reported recurrent homozygous deletions in *MAP2K3*, *MAP2K4*, *PTEN*, *CDKN2A/B*, *RB1*, and *ARID1A* and high-copy amplifications in *MDM4*, *MYC*, *CCND1*, *TERT*, and *FGF19* (13, 15, 16). We evaluated mouse SCNAs from WES data using Control-FreeC (40). Overall patterns of broad and focal alterations across the four mouse cohorts varied, with copy-number losses observed more often than gains. The only large recurrent chromosomal alteration in mouse (>25% of the chromosome arm) was copy loss of 14q in the MUP model (*SI Appendix*, Fig. S4*A*). We also identified deletions affecting *Rb1* (14qD3; 9% of mouse tumors) and *Cdkn2a* (4qC4; 5% of mouse tumors) across the four mouse models and amplifications affecting *Myc*, *Tert*, and *Vegfa* (Fig. 2*C*). Only SCNAs in which the expression of the gene relative to the median value for the model was consistent with the direction of the SCNAs were considered drivers (*Methods*). Other common human SCNAs, including deletions in *ERRFI1* (13% of human tumors) and *NCOR1* (22% of human tumors) and amplification of *CCND1* (6% of human tumors), were not observed in any of the mouse tumors.

Alteration of Pathways. Pathway analysis in human HCC has previously implicated WNT signaling, receptor tyrosine kinase (RTK)/PI3K kinase signaling, and cell-cycle signaling in HCC oncogenesis (14, 16). To determine whether partial overlap in mutated HCC genes between human and mouse models could imply perturbation of similar pathways in mouse liver tumorigenesis, we aggregated mutations from each model on these human HCC pathways. In addition to key pathways described in previous human HCC studies, we included elements of the MAPK pathway implicated by mutation frequency in mouse tumors (e.g., *Braf* in DEN mice) (Fig. 3). The mutation rate of a pathway was calculated as the fraction of tumors that harbored a likely driver mutation in one or more genes of the pathway. Among human tumors, pathway mutation rates were fairly uniform across the four cohorts with the exception of WNT signaling, which was altered in only 8% of LINC-CN tumors but in ∼30–40% of samples in other human cohorts (*SI Appendix*, Fig. S4*B*). Overall, the pathways with the highest mutation rate in human HCC were cell cycle, WNT signaling, and the SWI/SNF complex, with other pathways covering less than 20% of tumors.

STAM mice had pathway mutation rates similar to those in humans for most pathways but had more alterations targeting RTK signaling and chromatin-modification genes (*SI Appendix*, Fig. S4*B*). Despite the low mutation rate of *Trp53*, the cell-cycle pathway was perturbed at a similar rate in human tumors and STAM mice, suggesting that mouse tumors may target the cell cycle through alternative mechanisms more often than through *TP53*. In contrast to STAM mice, DEN mice did not frequently harbor mutations in cell-cycle genes. Instead, DEN mice tended to have mutations in MAPK signaling and RTK signaling, with less frequent alterations in WNT signaling, chromatin remodeling, and SWI/SNF. We observed few mutations in the MUP mouse model, but the few observed mutations affected the RTK and SWI/SNF pathways. TAK1 mice had no somatic alterations affecting the genes most frequently altered in human and mouse HCC. Overall, these findings suggest a more prominent role for RTK signaling in mouse tumorigenesis and suggest that in the DEN model the dual activation of MAPK signaling and RTK signaling could promote tumor formation in the absence of point mutations to cell-cycle and Wnt genes.

In general, a single driver mutation is sufficient to perturb the activity of a pathway; thus, it is uncommon to observe more than a single driver per pathway in a tumor. By aggregating mutations from multiple tumors at the pathway level, we therefore expect that driver mutations should be mutually exclusive, with only one driver mutation per pathway per tumor (41–43). Mutual exclusivity (ME) is a signature of positive selection at the pathway level and implicates the pathway in the disease process. We therefore evaluated the ME of mutations within six pathways in Fig. 3 (cell cycle, WNT pathway, MAPK pathway, RTK/RAS/PI3K pathway, chromatin modifiers, and the SWI/SNF complex) using a groupwise DISCOVER test (Dataset S1*C*) (41). Human patients showed significant ME of mutations affecting all six pathways, consistent with the established role of these pathways in HCC pathogenesis and confirming that mutations retained after removing likely passengers are enriched for driver events. Applying this analysis to mouse HCC samples, we found that among STAM tumors five of the six pathways (all but MAPK signaling) showed significant patterns of ME. In contrast, DEN tumors showed no significant ME of mutations in the six pathways. The DISCOVER test is intended to detect ME across pathway genes; however, nearly all MAPK mutations in DEN tumors were in a single gene (*Braf*). TAK1 and MUP models had too few mutations in genes belonging to the pathways considered to produce robust results.

To aid in the future development of mouse models recapitulating similar molecular alterations to human HCC, we evaluated patterns of ME mutation among the major HCC driver genes, focusing on the 13 genes identified as mutated above expected background levels. At an FDR <0.05, we observed ME between 12 gene pairs involving 10 of the 13 significantly mutated genes (Dataset S1*D*). *TP53* mutations were mutually exclusive with mutations to *CTNNB1*, *ALB*, *BAP1*, and *RPS6KA3*, while *CTNNB1* mutations were mutually exclusive with *TP53*, *AXIN1*, *RB1*, and *BAP1*. *AXIN1* mutations were mutually exclusive with *ALB*, *ACVR2A*, *KEAP1*, and *BAP1* mutations, and *BAP1* mutations also tended not to coincide with

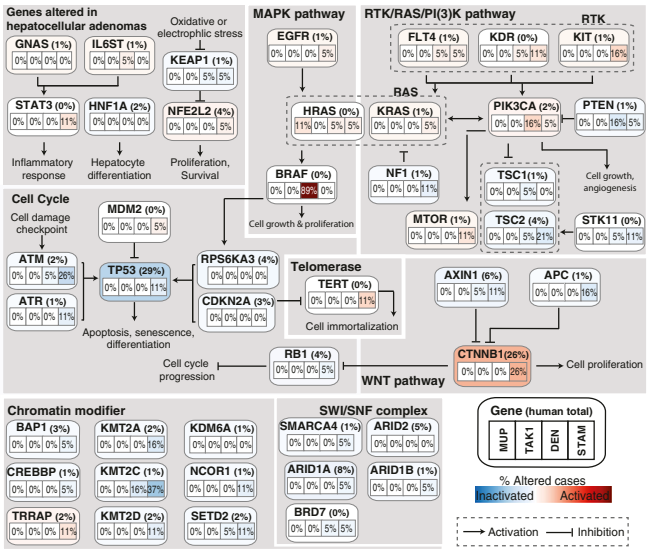

Fig. 3. Comparison of somatic alterations across HCC signaling pathways. Somatic mutations are indicated as the percentages of altered cases. Frequencies across four human cohorts are indicated as a single percentage to the right of the gene name (human gene nomenclature is used), while frequencies in the four mouse models are indicated separately by cells inside each gene. Missense mutations were included only if they were likely drivers (*Methods*). Genes are grouped by signaling pathways, with arrows and terminated lines indicating the direction and effect of gene activity within the pathway. (See key at in the lower right corner.)

ARID1A mutations. These patterns are consistent with human HCC being predominantly driven by deficiency of a factor associated with cell-cycle progression (*TP53*, *RB1*, and *RPS6KA3*) or by major regulators of the Wnt signaling pathway (*CTNNB1* and *AXIN1*) and suggest that secondary mutations such as those observed in *KEAP1*, *ARID1A*, or *ALB* may be biased by the primary driver pathway. Extending this analysis to include SCNAs (*Methods*), we observed additional ME between deletion of *RB1* and amplification of *MYC* and between deletion of *PTEN* and mutation of *CTNNB1*.

Transcriptomic Characterization. Transcriptomic changes reflect the cumulative effects of the genomic and epigenomic alterations that accumulate in cancer cells. Thus, we compared RNA-sequencing (RNA-seq)–derived transcriptomic similarity of human HCCs (n = 371) from TCGA and the 56 mouse tumor samples. Mouse tumors clustered predominantly according to mouse model; STAM and DEN samples were mostly isolated in single clusters, while TAK1 and MUP samples formed distinct but overlapping clusters. This configuration suggests that the largest differences in transcription across mouse HCC samples result from differences in etiology, especially for the DEN and STAM models, and their characteristic genetic aberrations (*SI Appendix*, Fig. S5*A*).

To determine whether tumor transcriptional profiles were similar among human tumors and mouse models, we calculated pairwise correlations between the gene-expression profiles of all mouse tumors with the core TCGA 196 human HCCs and 50 matched normal liver samples, restricting our analysis to the top 800 genes that are characteristically expressed in human HCC (*Methods*). We then clustered human samples according to their similarity to mouse tumors (Fig. 4). The majority of human normal liver samples clustered as a distinct group which included a small subset of human HCC samples. These samples fell within a larger cluster of tumors that was designated "H1." Two additional larger clusters of tumors were apparent and were designated "H2" and "H3," with H3 being the largest cluster. Each of these clusters could be further partitioned into subclusters (H1a, H1b, H1c, H2a, H2b, H3a, H3b, and H3c). We further annotated human and mouse tumors with proliferative status, as determined from expression of a gene set associated with cell proliferation (*SI Appendix*, Fig. S5*B*) (44).

Since this clustering was the result of human–mouse transcriptome similarities, we sought to determine if these clusters contained any biologic or clinical correlates that could define them and therefore explain the basis of the interspecies similarities (Dataset S2). H1, and particularly the subgroup interspersed with normal samples (H1a), was enriched for lower-grade tumors, tumors with low expression of proliferative genes, and had a very low prevalence of *TP53* mutations. H1 was also enriched in previously characterized Hoshida clusters C1 and C3, as well as TCGA iCluster 2. H2 was comprised predominantly of male tumor samples, and H2 tumors were characterized by low expression of proliferative genes, silencing of *CDKN2A*, and mutations in *CTNNB1*. Hoshida 3 was the predominant expression-based subtype associated with H2. Finally, H3 was enriched for high-grade tumors, tumors with high expression of proliferative genes, and *TP53* mutations. Hoshida 1 and 2 as well as iCluster 1 and 2 defined H3. We observed no association between clusters and HCC risk-related exposures, including alcohol consumption, HBV/HCV infection, cirrhosis, or smoking. However, we did observe a bias for male tumors to be enriched for alcohol consumption as well as *CTNNB1* and *TP53* mutations (Fisher's exact test; $P < 0.01$).

The characterization of these clinically and molecularly defined human HCC clusters allowed their meaningful mapping to mouse models to interpret similarities between human clusters and mouse models. The STAM model displayed the highest general correlation with cluster H3 and the lowest correlation with H1. Two-thirds of samples were highly correlated with H3a and had low correlation with all other clusters. The other third of the samples divided into two groups, one enriched in *Ctnnb1* mutations with high correlation with H2b and another with additional similarity to H2a and H1. DEN samples did not show strong similarity with any human cluster, with most samples displaying medium correlation to normal samples and H1/H2. The TAK1 model had the highest correlation with normal human liver samples while showing medium correlation with H1 and H2. Most MUP samples showed high correlation with normal and H1 groups with low correlation

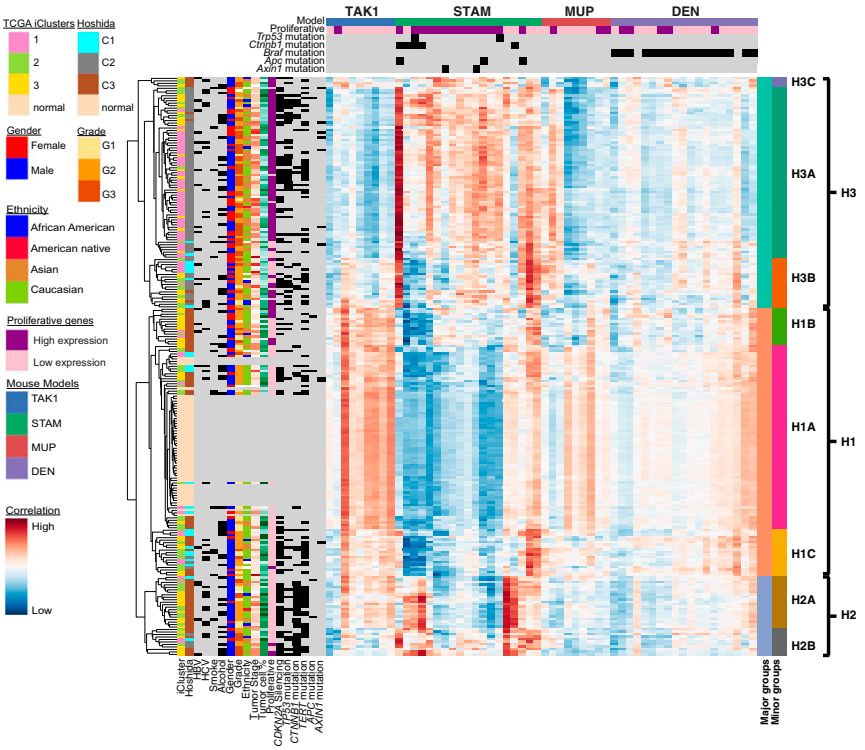

Fig. 4. Pairwise correlations between mouse tumors and human HCCs based on gene-expression profiles. Human clusters are indicated by the color bar on the right side of the heatmap, and the mouse models are indicated by the color bar above the heat map. Mutations for selected HCC genes in mouse tumors are shown above the heat map. A dendrogram of human HCCs and matched normal liver samples clustered according to correlation with mouse tumors based on the expression of 800 HCC-related genes is shown on the left. Clusters are labeled on the right side of the heatmap. Also left of the heatmap is a panel with clustering assignments (iCluster and Hoshida cluster), relevant environmental exposures (smoking history, alcohol), and clinical (gender, ethnicity, tumor grade, tumor stage, tumor cell purity) and molecular (*CDKN2A* silencing and mutation status of *TP53*, *CTNNB1*, *TERT*, and proliferative status) details for the 194 HCC patients. In the heatmap, red represents higher correlation, and blue shows lower correlation between a human sample and a mouse tumor.

with H2 or H3. Only two MUP samples showed high correlation with H3 and low correlation with normal samples.

The clustering of STAM tumors with high-grade proliferative and *TP53* mutation-enriched H3 HCCs versus *CTNNB1* mutation-enriched H2 HCCs suggested the possibility of shared patterns of gene expression downstream of inactivated *TP53* or activated *CTNNB1*. Indeed, 10 *TP53*-response genes, 13 *CTNNB1*-response genes, and 7 WNT pathway genes numbered among the 800 HCC-associated genes used for evaluating sample correlation. When mouse tumors were ranked according to the expression of *TP53*-response genes, STAM models were associated with higher activity of six genes inactivated by *TP53* (mouse orthologs of *CCNB1*, *CCNB2*, *CDK1*, *EZH2*, *FOXM1*, and *PLK1*) ($P < 0.01$), suggesting that *TP53* activity is frequently impaired in this model despite the paucity of *TP53* mutations (*SI Appendix*, Fig. S5*C*). Interestingly, STAM tumors with *Ctnnb1* mutations had similar patterns of downstream expression, but tumors with mutations to *Apc* appeared to have the highest overall expression of *CTNNB1*/WNT-response genes. STAM tumors with neither *Ctnnb1* nor *Apc* mutations were more highly correlated with H3 tumors and had higher overall expression of a subset of genes including *Loxl2*, *Cd14*, *Spp1*, and *Mmp14* that were expressed at low levels in the *CTNNB1* mutant STAM samples that had high correlation with H2 but low correlation with H3 (*SI Appendix*, Fig. S5*D*).

In summary, TAK1 and MUP tumors were most similar to low-grade human tumors, with a small number of MUP tumors beginning to show characteristics of higher-grade tumors to which the STAM model was the most similar. Notably, the DEN model does not appear to recapitulate the expression signature of any human tumors well. Overall, these results demonstrate that the integration of human molecular and clinical data with mutational and transcriptomics data from mouse models allows useful mapping of mouse models to the most suitable subgroups of patients.

Immune Signatures. The role of the immune system in cancer initiation, development, and clinical manifestation has recently taken center stage because of the demonstrated potential for immune manipulation to generate strong positive therapeutic outcomes (45). Human HCCs were reported to differ ostensibly in the immune cell content of their tumor (20); some tumors were characterized by high levels of immune cell infiltrate, while others were almost devoid of immune cells, and the cellular composition of the immune infiltrate differed substantially across tumors. Indeed, the important effects that inflammation-induced B cells exert on HCC development were recently revealed in the Mup-uPA HFD and STAM models by inhibiting T cell immune surveillance (40), demonstrating that mouse models can be effective for studying mechanisms of antitumor immunity and pointing to new therapeutic strategies to unleash robust immune responses. We therefore assessed the characteristics of the immune infiltration in the four mouse models of HCC from expression levels of immune marker genes to evaluate similarities among models and with human HCC.

We estimated the relative abundance of nine immune cell types in human and mouse tumors based on the expression of established cell type-specific markers previously used for this purpose (Fig. 5*A*) (46). Levels of mature CD4 T cells, T regulatory cells, and dendritic cells were comparable in human and mouse tumors. In contrast, mouse tumors had lower levels of CD8 T cells, natural killer cells, and B cells but higher levels of all types of macrophages. Consistent with lower CD8 T cell levels, we observed lower levels of cytotoxicity, as approximated from granzyme A and perforin expression (47), in mouse tumors than in human HCCs (Fig. 5*B*). Cytotoxicity did not correlate with mutation burden across mouse or human tumors (*SI Appendix*, Fig. S5*E*). We did not observe major differences in immune cell infiltrates when comparing mouse models (*SI Appendix*, Fig. S5*F*), suggesting that the molecular differences among the four models do not result in systematic differences in immune infiltration.

Innate and adaptive immunity can strongly promote or suppress cancer initiation, progression, and dissemination. Importantly, T cell-mediated elimination of cancer cells depends strictly on their T cell receptor specifically recognizing an MHC-I–bound neoantigen on cancer cells. We recently reported that the individual genotype of the HLA locus that encodes MHC-I imposes a restriction on which cancer-driver mutations are more likely to arise during carcinogenesis. This restriction results in a personal blind spot to specific driver mutations generated as a consequence of the different binding patterns displayed by the more than 3,000 human MHC-I alleles. Using the best rank (BR) mutation presentation scoring scheme that we previously developed and the same sets of driver and passenger mutations that we defined based on human tumors (48), we compared BR score distributions for driver and passenger mutations across different mammalian species' MHC-I alleles [$P < 1.0e\text{-}5$ for all except pig (*Sus scrofa*)], confirming that the general trend of higher presentation for cancer-driving mutations is evolutionary conserved (Fig. 5*C*).

We next focused the analysis on HCC patients' MHC-I alleles and mutations. We used the Patient Harmonic-mean Best Rank (PHBR) score (48) to estimate the genotype-specific immune presentation of mutations. Again, when we compared the score distribution of drivers and passengers found in HCC patients, there was a significantly higher score for HCC driver mutations ($P < 0.05$) (Fig. 5*D*). Interestingly, we observed the same trend when we considered mouse HCC mutations and alleles, suggesting that the mouse MHC-I genotype exerts constraints in HCC development similar to those found in human. These observations indicate that the mouse MHC-I genotype can have a strong influence in selecting the driving mutations that a given mouse model will develop. Since different mouse strains commonly used in preclinical cancer models have completely different sets of MHC-I alleles, it could be that the same cancer model can present different mutations depending on the genetic background. To analyze this possibility, we calculated PHBR scores for all mutations found in the four mouse models, considering the C57BL/6 or BALB/C strains for which binding predictions can be obtained. The C57BL/6 strain has the MHC-I b allele for H-2K and H-2D and is null for H-2L. The BALB/C strain has the d allele for all three loci. PHBR distributions show a significantly higher PHBR bias for C57BL/6 mice ($P < 0.01$), indicating that if tumor samples had been obtained from BALB/C mice instead of C57BL/6 mice the mutational content might have been different (Fig. 5 *E* and *F*), perhaps because of the additional H-2L alleles. Taken together these results suggest that the C57BL/6 background with only two homozygous MHC-I alleles could be driving the lower CD8 infiltration and cytotoxic activity observed in mice as compared with humans.

Discussion

HCC mouse modeling has historically relied heavily on the use of a variety of hepatotoxins that efficiently induce liver tumors in rats and mice. However, the genetic make-up of these tumors remains unknown, and therefore their validity in faithfully modeling human HCC is uncertain. An outstanding difficulty in mouse modeling of human HCC is the universal link with cirrhosis and the diverse conditions associated with the development of liver disease. Recent genomic analyses have uncovered an unexpected complexity in the genetics of HCC that hampers a direct translation into mice using conventional transgenesis (49). All these antecedents have contributed to the accumulation of a great number of mouse models of HCC generated by a large variety of chemicals, genetic engineering, dietary factors, and administration regimes (24, 50). Now it is quite unusual to find two independent studies in which the same model or regime for inducing mouse HCC is employed. To mitigate this extraordinary diversity in HCC experimental models that hampers advances in the field, we performed a systematic investigation of the similarities and differences between human HCCs and four mouse models of HCC at the genomic and transcriptomic scales. This study provides a molecular reference for tailoring the use of HCC mouse models to a specific experimental hypothesis or clinical testing.

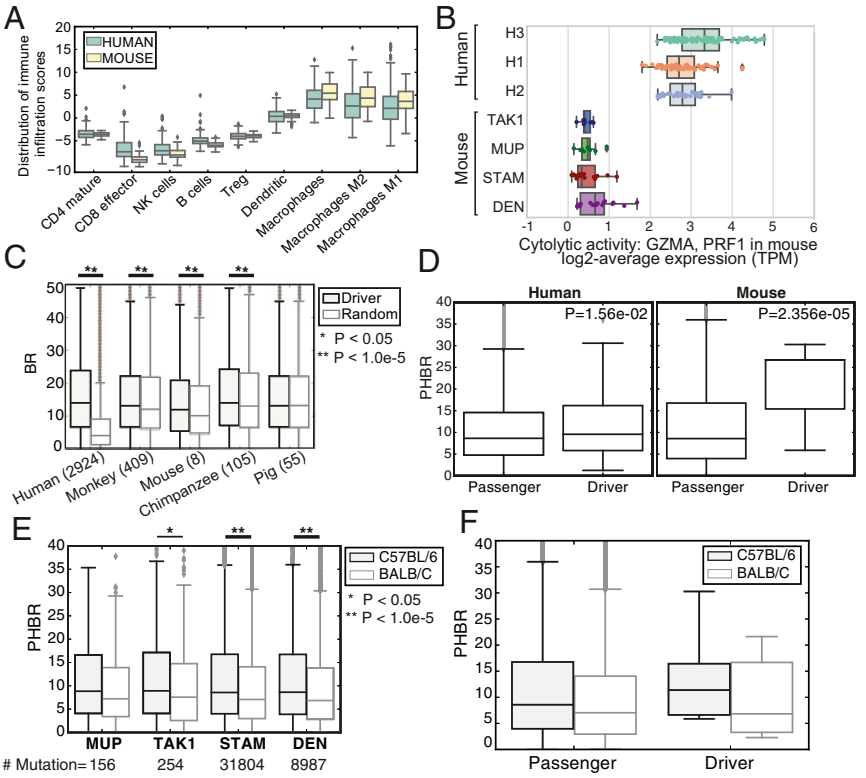

Fig. 5. Immune activities for human and mouse. (*A*) Immune infiltration scores for nine immune cell types in mouse and human tumors. (*B*) Cytolytic activities [log2-average expression (transcripts per million)] of GZMA and PRF1 of the mouse models and human clusters. (*C*) BR MHC-I presentation score distribution of driver mutations (inferred from frequency in human tumors) compared with random mutations in different species with number of alleles shown in parentheses. (*D*) PHBR score distributions for HCC driver mutations versus passenger mutations observed for human (n = 182 for driver and n = 28,216 for passenger) (*Left*) and mouse (n = 27 driver and n = 44,601 passenger) (*Right*). (*E*) PHBR score distributions for observed mutations for MHC-I alleles of C57BL/6 and BALB mouse models. (*F*) PHBR distribution of observed HCC driver and random mutations for MHC-I alleles of C57BL/6 and BALB mouse models.

Mutation signature analysis revealed subtle differences across human cohorts. However, among the four mouse models there was large variation in signatures suggesting major differences in DNA-damage mechanisms and mutation rates. DEN-induced tumors had an expected high mutation rate with a unique mutation signature that has never been observed in human cancer. STAM-induced tumors surprisingly contained an even higher mutational rate than would be expected of a very potent hepatotoxin. The mechanisms of carcinogenesis in the STAM model have been attributed to streptozotocin-induced diabetes combined with an HFD, thought to induce severe chronic liver injury leading to rapid HCC development. Our findings suggest that streptozotocin is also a potent liver carcinogen with a distinct alkylating mutational signature. Notably, STAM mice do not develop tumors unless liver damage is subsequently induced by an HFD. Since streptozotocin is an approved antineoplastic agent, we speculate that patients treated with this drug may benefit from preventive screening for HCC, particularly upon subsequent liver injury. Mutation signature clustering showed that TAK1- and MUP-induced tumors present signatures similar to human HCC. This observation indicates that long-term chronic liver damage without any carcinogen typical of these two models activates mechanisms of mutagenesis similar to those observed in patients who suffer from chronic liver disease. Taken together, these analyses show that mouse models of HCC based on administration of mutagens are not adequate models to study tumor initiation and mutational processes observed in human HCC. However, mouse models based on the spontaneous development of tumors after long-lasting liver injuries tend to recapitulate more faithfully the mutational processes observed in human HCC patients, as was previously postulated for MUP-uPA + HFD (40).

Contrary to the mutation signature analysis, gene and pathway-centric analysis determined that TAK1 and MUP tumors lacked oncogenic mutations and pathway alterations typically observed in human HCC. Molecular characteristics of the DEN model included mutations to the MAPK pathway, almost universally the equivalent of *BRAF* V600E, and frequent alterations to PI3K signaling. In a recent mouse study of DEN-induced HCC, Connor et al. (51) similarly reported that recurrent *Braf* mutation was the predominant driver in C57BL/6 mice. Of note, *TP53* and *CTNNB1*, the most frequently altered genes in human, were never found mutated in DEN-induced tumors. The DEN model thus results in tumors that are clearly distinct and different from human HCC. STAM tumors, with their high mutation rate, represented the only model containing oncogenic mutations in the prototypical genes found mutated in human HCC, concomitantly altering the Wnt, cell-cycle, and chromatin-modification pathways. While STAM tumors carried *Ctnnb1* mutations at a rate comparable to human tumors, *Trp53* mutations were less frequent. Nonetheless, the STAM model was the only mouse model that closely recapitulated the molecular characteristics of human HCC.

Mutation data are by nature sparse, and therefore it is not appropriate to quantitatively measure the degree of similarity between mouse and human HCC. Thus we compared tumors evaluating similarity at the transcriptomic level. Clustering human and mouse tumors according to pairwise transcriptomic correlations and consideration of molecular and clinical features allowed the definition of groups of patients based on their similarity to mouse HCC tumors. The H1 human cluster, which includes normal and low-grade samples, is defined mainly by its similarity to TAK1 and, to a lesser extent, MUP tumors along with a few samples from the DEN and STAM models. Indeed, around 70% of tumors >2 mm in HFD-fed MUP-uPA mice were histologically reported to be adenomas, which

agrees with the lowest mutational load, lack of oncogenic mutations, and low general similarity to human HCC (27). The absence of oncogenic mutations in the TAK1 and MUP models and their high correlation with "normal-like" human tumors and normal human liver invalidates these models for clinical testing or analysis of tumor biology. The H2 human cluster, which is characterized by enrichment of *CTNNB1* mutations and silencing of *CDKN2A*, was defined by its similarity to half of the STAM tumors, including all *Ctnnb1*-mutated samples, as well as to TAK1 tumors, although at lower correlation values. Finally, cluster H3, characterized by high-grade tumors and enrichment in *TP53* mutations, was uniquely defined by its high correlation with all STAM samples. We observed a sex-specific bias toward males in the *CTNNB1* mutation-associated H2 tumor group (Dataset S2) and found that *CTNNB1* was more frequently mutated in male tumors. This raises the possibility of sex differences that could influence the molecular characteristics of tumors. Previous studies have suggested that the more frequent occurrence of HCC in men could be attributable to differences in environmental exposure (greater alcohol consumption, smoking, and higher body mass index) or hormone levels (16). Schulze et al. (15) also suggested that the mutation of *CTNNB1* in HCC is higher in cohorts with high levels of alcohol consumption. Interestingly, we found that *TP53* mutations were biased toward male tumors as well. We note that the mouse tumors studied here were almost universally derived from male mice, but we did not observe any bias for these samples to correlate more strongly with male or female tumors on the basis of the expression of the 800 HCC genes ($P >> 0.05$) (*SI Appendix*, Fig. S5*G*). This confirms that the transcriptional similarities observed among mouse and human tumors were not confounded by gender.

Antitumor immunity is emerging as an important research area, and mouse models are likely to play a central role in determining the optimal application of immunotherapy in HCC. Although we see evidence that the MHC-I genotype restricts mutations in tumors in mice a manner similar to its effect in humans, we nonetheless see differences in immune cell infiltration and corresponding differences in cytotoxicity. It is possible that these differences are rooted in the rate at with which mouse tumors develop (40) or could reflect differences in presentation associated with the diversity of HLA alleles carried by a particular strain. Specifically, the C57BL/6 genetic background of the tumor samples analyzed here includes only two homozygous HLA alleles, potentially reducing the breadth of peptides presented and therefore minimizing the substrate available to drive T cell infiltration and recognition. Interestingly, Connor et al. (51) found that DEN-induced mutations differed between mouse strains, with Braf mutations being more prevalent in the C57BL/6 mice while Hras and Egfr mutations were far more frequent in CH3 mice. We note that these two mouse strains carry different MHC genotypes, further suggesting that genetic background could be an important consideration when using mice to study tumor development and preclinical studies. Nevertheless, further work is needed to determine whether conclusions about immune response drawn from specific mouse models will generalize well to human disease.

In summary, we performed a comprehensive human–murine HCC molecular comparison to determine the similarity of a given mouse model to different subgroups of patients. We analyzed four different models ranging from carcinogen treatment to genetic induction of chronic liver injury. Our results indicate that mouse models spontaneously inducing HCC through chronic liver damage tend to be most similar to human HCC in terms of mutational processes, but these tumors tend to be low grade with a very low frequency of the oncogenic mutations typically found in standard human HCC. Thus, these models appear to be suitable only for studying HCC initiation or microenvironmental determinants of mutational processes. In contrast, our analysis indicated that the STAM model is the most suitable model for research on tumor biology and preclinical studies. Despite its high mutational burden and biased mutation signatures, it generates tumors most molecularly similar to high-grade human HCC and to human tumors with the *CTNNB1* mutation. Our results also indicate that, in general, the DEN model should be avoided as a model of human HCC because it is dominated by mutational mechanisms that are never found in human cancer, and DEN-induced tumors have a molecular profile that is clearly different at the gene, pathway, and transcriptomic levels from the other models analyzed. Of note, we also found that the genetic background of the mice can have an impact on the molecular characteristics of the tumors that develop based on the mouse strain-specific MHC-I genotype. In conclusion, we expect that these analyses will help the HCC field to better tailor experimental analysis to the most adequate mouse models and at the same time serve as an initial workflow by which additional mouse models can be reliably characterized.

Methods

Samples. Mouse studies were performed in accordance with the NIH *Guide for the Care and Use of Laboratory Animals* (52) and were approved by the University of California, San Diego Institutional Animal Care and Use Committee, S00218. All mice used were of the C57BL/6 background. Tumors >4 mm were excised from all mice without any other consideration to avoid biases. TAK1 samples consisted of nine tumors and three spleens from five 9-mo-old Alb-Cre; Tak1F/F mice (25, 26). MUP samples (one spleen and nine tumors) were obtained from five MUP-uPA male mice fed with an HFD as previously reported (27). DEN samples (19 tumors and one spleen) were obtained from eight male mice injected with DEN at postnatal day 15 as previously described (24, 25). STAM samples (one spleen and 19 tumors) were obtained from six male mice treated with streptozotocin at postnatal day 2 and fed with HFD as previously described (28). DNA and RNA were extracted and purified with the Qiagen AllPrep DNA/RNA Mini Kit. Exome capture and sequencing were performed at the University of California, San Diego (UCSD) genomics core for TAK1, DEN, and STAM samples; MUP samples were processed at Beijing Genomics Institute. RNA-seq for all samples was performed at the UCSD genomics core.

Allele-Based Immune Presentation Analysis. To evaluate the conservation of immune presentation across species, we compared immune presentation scores for driver and random mutations as described in Marty et al. (48) across all alleles present in the Immune Epitope database (IEDB) for several species: mouse (*Mus musculus*), chimpanzee (*Pan troglodytes*), gorilla (*Gorilla gorilla*), and pig (*S. scrofa*). The 1,018 driver mutations were mapped to their orthologous position in mouse (*M. musculus*, *GRCm38*), monkey (*Rhesus macaque* or *Macaca mulatta*, *Mmul_8.0.1*), chimpanzee (*P. troglodytes*, *Pan_tro3.0*), and pig (*S. scrofa*, *Sscrofa11.1*) using liftOver. Random mutations ($n = 10{,}000$) were generated for each species by sampling random positions from the protein fasta downloaded from the Ensembl Release 91 databases (ftp://ftp.ensembl.org/pub/release-91/) and creating random amino acid changes. Each HLA allele–mutation pair was assigned an immune presentation score using the BR formulation computed from affinities predicted by NetMHCpan3.0 (53). Only classic alleles from each species are considered. BR scores (48) across 2,924 human alleles, 409 monkey alleles, 8 mouse alleles, 105 chimpanzee alleles, and 55 pig alleles were calculated for the 1,018 driver mutations and 10,000 random mutations. Across categories, this resulted in 38.7 million residue scores (human: 2,924,000 driver, 29,210,000 random; mouse: 7,416 driver, 80,000 random; chimpanzee: 101,220 driver, 1,050,000 random; gorilla: 397,155 driver, 4,150,000 random; pig: 69,750 driver, 750,000 random). BR scores were then pooled across HLAs.

PHBR Score. PHBR scores (48) were calculated for mutations observed in human and mouse models, and distributions were compared between driver and passenger mutations within each species. Observed mutations were considered drivers if they overlapped the 1,018 driver mutations from the human pan-cancer study (48), and the remainder of the mutations were considered passengers (human: 182 driver, 28,216 passenger; mouse: 27 driver, 44,601 passenger). Within each species, the difference in the distribution of PHBR scores for drivers versus passenger mutations was evaluated using the Wilcoxon rank-sum test.

We also evaluated the effect of mouse strain-specific MHC-I genotypes on PHBR score distributions for driver and passenger mutations. The mouse models in the current study are from the C57BL/6 strain, which carries the k allele for H-2K and H-2D and is null for H-2L. We compared presentation by the C57BL/6 genotype with presentation by the BALB/C genotype, which consists of the d allele for all three HLA loci using the Wilcoxon rank-sum test.

Parametric and nonparametric statistics tests were used to analyze significance of results, including Wilcoxon rank-sum test to evaluate enrichment, TP53 and CTNNB1activities, and the distributions of driver and passenger mutations. We

applied multiple testing corrections (Benjamini–Hochberg) to adjust for the P values. A single asterisk signifies $P < 0.05$ unless otherwise noted.

Details are found in *SI Appendix, Supplementary Methods*.

ACKNOWLEDGMENTS. This research was supported by NIH Grants CA118165, AI043477, U01AA022614, and P42ES010337 (to M.K.), DP5-OD017937 (to H.C.), K99/R00CA191152 (to J.F.-B.), and R01DK085252 (to E.S); Moores Cancer Center Support Grant P30CA023100 (to O.H.); a grant from Bristol-Myers Squibb (to K.T.); NIH National Library of Medicine Training Grant T15LM011271 (to M.D.); National Science Foundation Graduate Fellowship 2015205295 (to R.M.P.); a Canadian Institute for Advanced Research fellowship (to H.C.); Japan Society for the Promotion of Science Grant-in-Aid for Scientific Research Grant JP15K21775 (to K.T.); the "Kibou Projects" Startup Support for Young Researchers in Immunology (K.T.); the Irvington Cancer Research Institute (S.S.); a Prostate Cancer Foundation Young Investigator Award (to S.S.); and a Southern California Research Center for ALPD and Cirrhosis grant (to S.S.). M.K. holds the Ben and Wanda Hildyard Chair for Mitochondrial and Metabolic Diseases endowed by the University of California San Diego School of Medicine. The results published here are based in part upon data generated by TCGA managed by the National Cancer Institute and the National Human Genome Research Institute. Information about TCGA can be found at https://cancergenome.nih.gov/.

1. Ferlay J, et al. (2015) Cancer incidence and mortality worldwide: Sources, methods and major patterns in GLOBOCAN 2012. *Int J Cancer* 136:E359–E386.
2. El-Serag HB, Rudolph KL (2007) Hepatocellular carcinoma: Epidemiology and molecular carcinogenesis. *Gastroenterology* 132:2557–2576.
3. Bosch FX, Ribes J, Cléries R, Díaz M (2005) Epidemiology of hepatocellular carcinoma. *Clin Liver Dis* 9:191–211.
4. Holmberg SD, Spradling PR, Moorman AC, Denniston MM (2013) Hepatitis C in the United States. *N Engl J Med* 368:1859–1861.
5. El-Serag HB, Davila JA (2011) Surveillance for hepatocellular carcinoma: In whom and how? *Therap Adv Gastroenterol* 4:5–10.
6. Ascha MS, et al. (2010) The incidence and risk factors of hepatocellular carcinoma in patients with nonalcoholic steatohepatitis. *Hepatology* 51:1972–1978.
7. Llovet JM, et al. (2016) Hepatocellular carcinoma. *Nat Rev Dis Primers* 2:16018.
8. Wilhelm SM, et al. (2008) Preclinical overview of sorafenib, a multikinase inhibitor that targets both Raf and VEGF and PDGF receptor tyrosine kinase signaling. *Mol Cancer Ther* 7:3129–3140.
9. Llovet JM, et al.; SHARP Investigators Study Group (2008) Sorafenib in advanced hepatocellular carcinoma. *N Engl J Med* 359:378–390.
10. Bruix J, et al.; RESORCE Investigators (2017) Regorafenib for patients with hepatocellular carcinoma who progressed on sorafenib treatment (RESORCE): A randomised, double-blind, placebo-controlled, phase 3 trial. *Lancet* 389:56–66.
11. El-Khoueiry AB, et al. (2017) Nivolumab in patients with advanced hepatocellular carcinoma (CheckMate 040): An open-label, non-comparative, phase 1/2 dose escalation and expansion trial. *Lancet* 389:2492–2502.
12. Hoshida Y, et al. (2009) Integrative transcriptome analysis reveals common molecular subclasses of human hepatocellular carcinoma. *Cancer Res* 69:7385–7392.
13. Ahn S-M, et al. (2014) Genomic portrait of resectable hepatocellular carcinomas: Implications of RB1 and FGF19 aberrations for patient stratification. *Hepatology* 60: 1972–1982.
14. Guichard C, et al. (2012) Integrated analysis of somatic mutations and focal copy-number changes identifies key genes and pathways in hepatocellular carcinoma. *Nat Genet* 44:694–698.
15. Schulze K, et al. (2015) Exome sequencing of hepatocellular carcinomas identifies new mutational signatures and potential therapeutic targets. *Nat Genet* 47:505–511.
16. Totoki Y, et al. (2014) Trans-ancestry mutational landscape of hepatocellular carcinoma genomes. *Nat Genet* 46:1267–1273.
17. Letouzé E, et al. (2017) Mutational signatures reveal the dynamic interplay of risk factors and cellular processes during liver tumorigenesis. *Nat Commun* 8:1315.
18. Fujimoto A, et al. (2016) Whole-genome mutational landscape and characterization of noncoding and structural mutations in liver cancer. *Nat Genet* 48:500–509.
19. Zhang J, et al. (2011) International Cancer Genome Consortium Data Portal–A one-stop shop for cancer genomics data. *Database (Oxford)* 2011:bar026.
20. Cancer Genome Atlas Research Network (2017) Comprehensive and integrative genomic characterization of hepatocellular carcinoma. *Cell* 169:1327–1341.
21. Santos NP, Colaço AA, Oliveira PA (2017) Animal models as a tool in hepatocellular carcinoma research: A review. *Tumour Biol* 39:1010428317695923.
22. Lee J-S, et al. (2004) Application of comparative functional genomics to identify best-fit mouse models to study human cancer. *Nat Genet* 36:1306–1311.
23. Nakagawa H (2015) Recent advances in mouse models of obesity- and nonalcoholic steatohepatitis-associated hepatocarcinogenesis. *World J Hepatol* 7:2110–2118.
24. Heindryckx F, Colle I, Van Vlierberghe H (2009) Experimental mouse models for hepatocellular carcinoma research. *Int J Exp Pathol* 90:367–386.
25. He G, et al. (2013) Identification of liver cancer progenitors whose malignant progression depends on autocrine IL-6 signaling. *Cell* 155:384–396.
26. Inokuchi S, et al. (2010) Disruption of TAK1 in hepatocytes causes hepatic injury, inflammation, fibrosis, and carcinogenesis. *Proc Natl Acad Sci USA* 107:844–849.
27. Nakagawa H, et al. (2014) ER stress cooperates with hypernutrition to trigger TNF-dependent spontaneous HCC development. *Cancer Cell* 26:331–343.
28. Fujii M, et al. (2013) A murine model for non-alcoholic steatohepatitis showing evidence of association between diabetes and hepatocellular carcinoma. *Med Mol Morphol* 46:141–152.
29. Szikriszt B, et al. (2016) A comprehensive survey of the mutagenic impact of common cancer cytotoxics. *Genome Biol* 17:99.
30. Alexandrov LB, Nik-Zainal S, Wedge DC, Campbell PJ, Stratton MR (2013) Deciphering signatures of mutational processes operative in human cancer. *Cell Rep* 3:246–259.
31. Forbes SA, et al. (2017) COSMIC: Somatic cancer genetics at high-resolution. *Nucleic Acids Res* 45:D777–D783.
32. Alexandrov LB, et al. (2015) Clock-like mutational processes in human somatic cells. *Nat Genet* 47:1402–1407.
33. Ng AWT, et al. (2017) Aristolochic acids and their derivatives are widely implicated in liver cancers in Taiwan and throughout Asia. *Sci Transl Med* 9:eaan6446.
34. Blokzijl F, et al. (2016) Tissue-specific mutation accumulation in human adult stem cells during life. *Nature* 538:260–264.
35. Alexandrov LB, et al. (2016) Mutational signatures associated with tobacco smoking in human cancer. *Science* 354:618–622.
36. Vogelstein B, et al. (2013) Cancer genome landscapes. *Science* 339:1546–1558.
37. Lawrence MS, et al. (2013) Mutational heterogeneity in cancer and the search for new cancer-associated genes. *Nature* 499:214–218.
38. Greenman C, Wooster R, Futreal PA, Stratton MR, Easton DF (2006) Statistical analysis of pathogenicity of somatic mutations in cancer. *Genetics* 173:2187–2198.
39. Carter H, Samayoa J, Hruban RH, Karchin R (2010) Prioritization of driver mutations in pancreatic cancer using cancer-specific high-throughput annotation of somatic mutations (CHASM). *Cancer Biol Ther* 10:582–587.
40. Shalapour S, et al. (2017) Inflammation-induced IgA+ cells dismantle anti-liver cancer immunity. *Nature* 551:340–345.
41. Canisius S, Martens JWM, Wessels LFA (2016) A novel independence test for somatic alterations in cancer shows that biology drives mutual exclusivity but chance explains most co-occurrence. *Genome Biol* 17:261.
42. Ciriello G, Cerami E, Sander C, Schultz N (2012) Mutual exclusivity analysis identifies oncogenic network modules. *Genome Res* 22:398–406.
43. Vandin F, Upfal E, Raphael BJ (2012) De novo discovery of mutated driver pathways in cancer. *Genome Res* 22:375–385.
44. Andrisani OM, Studach L, Merle P (2011) Gene signatures in hepatocellular carcinoma (HCC). *Semin Cancer Biol* 21:4–9.
45. Mittal D, Gubin MM, Schreiber RD, Smyth MJ (2014) New insights into cancer immunoediting and its three component phases–Elimination, equilibrium and escape. *Curr Opin Immunol* 27:16–25.
46. Davoli T, Uno H, Wooten EC, Elledge SJ (2017) Tumor aneuploidy correlates with markers of immune evasion and with reduced response to immunotherapy. *Science* 355:355.
47. Rooney MS, Shukla SA, Wu CJ, Getz G, Hacohen N (2015) Molecular and genetic properties of tumors associated with local immune cytolytic activity. *Cell* 160:48–61.
48. Marty R, et al. (2017) MHC-I genotype restricts the oncogenic mutational landscape. *Cell* 171:1272–1283.e15.
49. Bakiri L, Wagner EF (2013) Mouse models for liver cancer. *Mol Oncol* 7:206–223.
50. Chen X, Calvisi DF (2014) Hydrodynamic transfection for generation of novel mouse models for liver cancer research. *Am J Pathol* 184:912–923.
51. Connor F, et al. (2018) Mutational landscape of a chemically-induced mouse model of liver cancer. *J Hepatol* 69:840–850.
52. National Research Council (2011) *Guide for the Care and Use of Laboratory Animals* (National Academies Press, Washington, DC), 8th Ed.
53. Nielsen M, Andreatta M (2016) NetMHCpan-3.0; improved prediction of binding to MHC class I molecules integrating information from multiple receptor and peptide length datasets. *Genome Med* 8:33.